Article

Fuzzy-Adaptive ESO Control for Dual Active Bridge Converters

Ju-Hyeong Seo and Sung-Jin Choi *

Department of Electrical, Electronic and Computer Engineering, University of Ulsan, Ulsan 44610,
Republic of Korea; chris3342@mail.ulsan.ac.kr
* Correspondence: sjchoi@ulsan.ac.kr

Abstract

In converter-dominated direct-current microgrids, severe load transients can cause large voltage deviations on the common direct-current bus. To mitigate this, an energy storage system is typically employed, and an isolated bidirectional dual active bridge converter is commonly used as the power interface. Therefore, the controller must ensure robust transient performance under step-load conditions. This paper proposes an active disturbance rejection control framework that adaptively adjusts the bandwidth of an extended state observer using fuzzy logic. The proposed observer increases its bandwidth during transients—based on the estimation error—to accelerate disturbance compensation, while decreasing the bandwidth near steady state to suppress noise amplification. This adaptive tuning alleviates the fixed-bandwidth trade-off between transient speed and noise sensitivity in ESO-based regulation. Hardware experiments under load-step conditions validate the method: for a load increase, the peak voltage undershoot and settling time are reduced by 22% and 48.9% relative to a proportional–integral controller, and by 20% and 36.1% relative to a fixed-bandwidth observer. For a load decrease, the peak overshoot and settling time are reduced by 27.9% and 49.5% compared with the proportional–integral controller, and by 20.5% and 25% compared with the fixed-bandwidth observer.

Keywords: active disturbance rejection control (ADRC); adaptive bandwidth; DC microgrids (DCMG); dual active bridge (DAB); extended state observer (ESO); fuzzy logic

1. Introduction

Recently, driven by carbon-neutrality targets and the efficiency requirements of power-electronics-dominated systems, DC microgrids (DCMGs) are gaining traction across applications such as data centers, transportation electrification, and industrial facilities [1]. Compared with ac distribution, DC architectures avoid frequency and phase synchronization requirements, reduce issues related to reactive-power flows and harmonics/unbalances, and interface naturally with renewable sources, power-electronic loads, and energy storage systems (ESS) [1,2]. In particular, in islanded or weakly grid-tied DCMGs, rapid variations in load and generation can induce deviations of the common DC-bus voltage; thus, tight regulation and fast restoration to the nominal reference become key control objectives for power quality and reliability [3–5]. To mitigate these power imbalances, an ESS is commonly integrated to buffer fast dynamics [6]. As a bidirectional power interface between the ESS and the DC bus, the dual active bridge (DAB), an isolated bidirectional DC/DC converter, is widely used [7,8]. The DAB offers high-frequency galvanic isolation, high power conversion efficiency over a wide operating range, and flexible power flow control through various modulation techniques such as single-phase-shift (SPS) and triple-phase-shift

(TPS) [9–14]. Moreover, accurate average and discrete models have been established [11], along with frequency-domain zero-voltage switching (ZVS) boundary analysis [12] and phase-shift control methods for achieving fast dynamic response [13,14]. These modulation and control design guidelines have been systematically presented, and their reliability in high-power applications has been experimentally validated [11–14]. However, in real DCMG environments, superimposed uncertainties—including bus-impedance variations, model mismatch, sensor noise and delay, and abrupt step-like load changes—make an inherent trade-off between the robustness and dynamic performance of the DAB controller unavoidable [3,10].

Traditionally, single-voltage-loop PI controllers are designed for a specific operating point. Therefore, under rapid load transients, the operating point shifts away from the design point, making it difficult to maintain optimal performance [14,15]. Model predictive control (MPC) offers the advantage of fast transient response; however, it has inherent limitations, including a high computational burden in high-switching-frequency and high-speed sampling environments, as well as sensitivity to model mismatches [16–20]. Conventional sliding mode control (SMC) offers high robustness and fast responsiveness; however, due to its discontinuous switching control, chattering can occur, which may degrade system performance and cause potential damage to mechanical components [21,22]. Therefore, active disturbance rejection control (ADRC), which reduces dependence on detailed models while maintaining fast transient response and robustness, has attracted attention as an alternative [23]. The core of ADRC, the extended state observer (ESO), can compensate for model uncertainties and disturbances by treating them as a single total disturbance, thereby simplifying the control structure [24,25]. However, ESO inherently presents a trade-off between dynamic performance and noise based on the observer bandwidth; increasing the bandwidth improves dynamic performance but simultaneously amplifies noise [8,26–28].

To address these limitations, this paper proposes a fuzzy logic-based ESO bandwidth adjustment method for the DAB converter. In this approach, fuzzy logic operates based on the estimation error to adaptively adjust the observer bandwidth of the ESO in real time. This method mitigates the drawbacks of the strong dependence of MPC on models and parameters, the fixed-gain trade-off of ADRC, and chattering in SMC, while enhancing both power quality and reliability under severe step-load transients in converter-dominated DC microgrids.

The main contributions of this paper are summarized as follows:

- A unified frequency-domain analysis of the fixed-bandwidth ESO for DAB voltage regulation is presented, clarifying the trade-off between low-frequency disturbance rejection (under operating-point/model mismatch) and high-frequency noise amplification.
- A fuzzy logic-based adaptive ESO (FESO) is proposed to tune the observer bandwidth online using the ESO estimation error, increasing it only during transients for faster disturbance compensation while reducing it near steady state to mitigate noise sensitivity.
- The proposed method is validated via sensitivity-based robustness analysis under operating-point variations and hardware step-load experiments, demonstrating reduced voltage deviation and shorter settling time compared with a PI controller and a conventional fixed-bandwidth ESO.

The structure of this paper is as follows: Section 2 discusses the principles of ADRC. Section 3 presents the DAB converter controller design methodology and explains the ESO bandwidth trade-off. Section 4 describes the proposed fuzzy logic-based bandwidth adjustment method. Section 5 verifies the performance of the proposed method through hardware experiments. Section 6 discusses the scope of the proposed local controller

and future research directions that consider communication constraints in distributed extensions. Finally, Section 7 concludes this paper.

2. Review of the ADRC Framework

Active disturbance rejection control (ADRC) models an n-th order system as an ideal n-th order integrator between the input and output, and separates it into a total disturbance that includes internal parameter uncertainties and external disturbances as shown in (1):

$$y^{(n)}(t) = f(t) + bu(t). \tag{1}$$

(1) can be expressed in a state-space form with an extended structure that includes the disturbance term. To estimate the total disturbance $f(t)$, the extended model can be reconstructed in the form of a Luenberger observer as shown in (2):

$$\begin{aligned} \dot{z} &= Az + Bu + L(\hat{y} - Cz) \\ \tilde{y} &= Cz \end{aligned}. \tag{2}$$

Here, $\hat{y}$ denotes the actual output, and $\tilde{y}$ represents the estimated output. The observer gain reacts to the difference between the measured output and the estimated value. Using this structure, an ESO (extended state observer) is constructed to estimate the lumped disturbance term.

The input $u(t)$ for compensating the estimated disturbance can be expressed as

$$u(t) = \frac{u_0(t) - z_{n+1}(t)}{b}. \tag{3}$$

If the disturbance is perfectly estimated such that $z_{n+1}(t) = f(t)$, substituting (3) into (1) yields the following simple n-th order integrator form:

$$y^{(n)}(t) = u_0(t). \tag{4}$$

The observer gains β_i are commonly designed via pole placement using a single observer bandwidth parameter ω_o as follows:

$$\beta_i = \binom{n+1}{i} \omega_o^i. \tag{5}$$

As shown in (6), all observer poles are determined by the observer bandwidth ω_o:

$$s^{n+1} + \beta_1 s^n + \beta_2 s^{n-1} + \cdots + \beta_{n+1} = (s + \omega_o)^{n+1}. \tag{6}$$

As a result, the roots of the characteristic equation are located at $-\omega_o$, which defines the dynamic performance of the observer:

$$(s + \omega_o)^{n+1} = 0. \tag{7}$$

As the poles move farther left in the left-half plane (LHP), the observer bandwidth increases, leading to faster convergence of the estimation error to zero. However, if ω_o becomes excessively large, the system becomes sensitive to noise and may suffer from limitations due to the sampling frequency. The detailed derivation of the ESO structure and pole-placement gain design is provided in Appendix A.

3. ADRC for the DAB Converter and Its Limitations

3.1. Controller Design for the DAB Converter

The DAB (Dual Active Bridge) converter consists of full-bridge circuits on both the input and output sides as shown in Figure 1, and these are connected through a transformer. According to [10], the reduced-order model is employed in this paper since it lowers the model complexity while still ensuring high large-signal and small-signal accuracy. In the reduced-order model, the system is approximated as a first-order transfer function with a single dominant pole. The resulting transfer function can be expressed as follows:

$$G_{vd}(s) = \frac{\hat{v}_o}{\hat{d}} = \frac{NV_i(1-2D)}{2f_sL} \cdot \frac{R_L}{R_LC_fs+1}. \tag{8}$$

Here, N is the turns ratio of the transformer, V_i is the input voltage, and D is the phase shift ratio, which typically ranges from 0 to 0.5. R_L denotes the load resistance, f_s is the switching frequency, C_f is the output capacitance, and L is the series inductance.
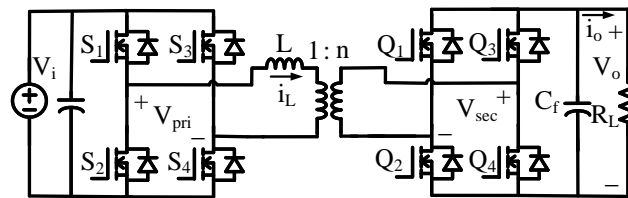

Figure 1. Schematic of the DAB converter.

To design the ESO, the transfer function in (8) is transformed into the time domain as

$$\frac{d\hat{v}_o}{dt} = -\frac{\hat{v}_o}{R_LC_f} + \frac{NV_i(1-2D)}{2f_sLC_f} \cdot \hat{d}(t). \tag{9}$$

Considering both internal and external uncertainties as a total disturbance, the system can be extended as

$$\frac{d\hat{v}_o}{dt} = -\frac{\hat{v}_o}{R_LC_f} + (b-b_0)\hat{d}(t) + b_0\hat{d}(t) \tag{10}$$

If we define the total disturbance as

$$f(t) = -\frac{\hat{v}_o}{R_LC_f} + (b-b_0)\hat{d}(t) \tag{11}$$

Then the structure becomes identical to that of (1).

Here, b represents the actual DAB converter parameter, and b_0 is the nominal parameter used in the design, which can be expressed as

$$b_0 = \frac{N_0V_{i0}(1-2D_0)}{2f_{s0}L_0C_{f0}}. \tag{12}$$

The input $d(t)$ is defined by (3). If the estimated disturbance is denoted as $\tilde{f}(t)$, then $\hat{d}(t)$ can be expressed accordingly as

$$\hat{d}(t) = \frac{\hat{d}_0(t) - \tilde{f}(t)}{b_0}. \tag{13}$$

Therefore, the ESO for the DAB converter can be derived from (A6) and is formulated as follows:

$$\dot{\hat{v}}_o = \tilde{f} + \beta_1(\hat{v}_o - \tilde{v}_o) + b_0\hat{d}$$
$$\dot{\tilde{f}} = \beta_2(\hat{v}_o - \tilde{v}_o). \tag{14}$$

Here, $\tilde{v}_o$ represents the estimated output voltage. If the disturbance is effectively estimated through the observer, the system can be simplified to a first-order integrator form as described in (4). Accordingly, control can be achieved using a simple proportional controller with gain ω_c. The structure of this observer can be illustrated using a block diagram as shown in Figure 2.
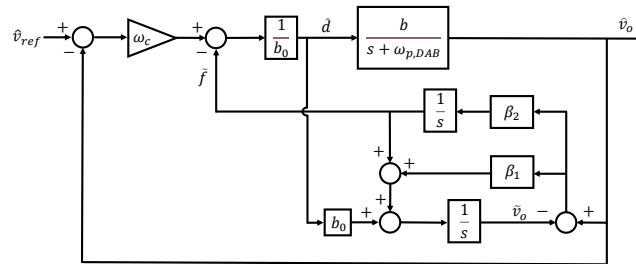

Figure 2. Block diagram of ESO system.

3.2. Limitation of the Conventional Method

By transforming (14) into the *s*-domain, the estimated disturbance value $\tilde{F}(s)$ can be expressed as

$$\tilde{F}(s) = \frac{\beta_2 s}{s^2 + \beta_1 s + \beta_2}\hat{V}_o(s) - \frac{\beta_2 b_0}{s^2 + \beta_1 s + \beta_2}\hat{D}(s). \tag{15}$$

If we choose $\beta_1 = 2\omega_o$ and $\beta_2 = \omega_o^2$, the observer gains β can be defined in terms of the observer bandwidth ω_o, as shown in (5). This relationship can also be represented using a block diagram, as illustrated in Figure 3a.
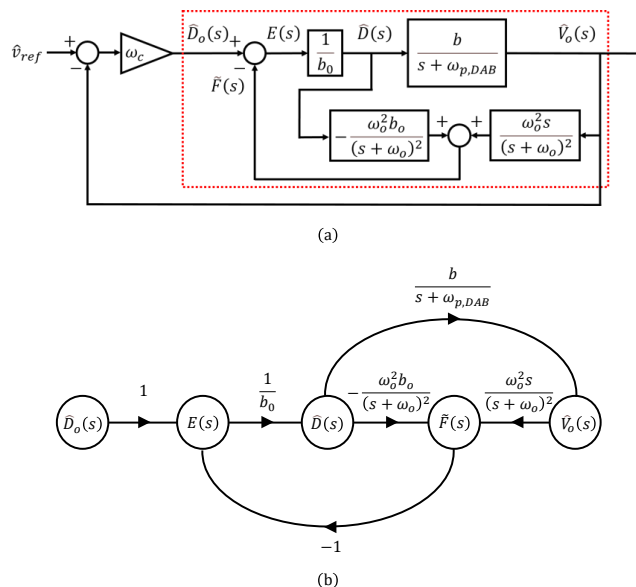

Figure 3. ADRC for DAB: (**a**) simplified diagram, (**b**) signal-flow graph for limitation analysis. The red dotted box indicates the ESO-based disturbance estimation and compensation subsystem.

By converting the red boxed region in the block diagram into a signal-flow graph as shown in Figure 3b and applying Mason's gain rule, the output $\hat{V}_o(s)$ with respect to the input $\hat{D}_o(s)$ can be expressed as follows:

$$G_{vdo}(s) = \frac{\hat{V}_o(s)}{\hat{D}_o(s)} = \frac{1}{K + \frac{2}{A}} \cdot \frac{1}{s} \cdot \frac{N_1(s)}{D_1(s)} \tag{16}$$

where,

$$N_1(s) = 1 + \frac{1}{Q_o}\left(\frac{s}{\omega_o}\right) + \left(\frac{s}{\omega_o}\right)^2 \tag{17}$$

$$D_1(s) = 1 + \frac{1}{Q_n}\left(\frac{s}{\omega_n}\right) + \left(\frac{s}{\omega_n}\right)^2. \tag{18}$$

The transfer function consists of an overall gain, an integrator, and second-order systems in both the numerator and the denominator. Here, we introduce two design parameters: $K = \frac{b}{b_0}$ represents the ratio of the designed parameter to the actual parameter, indicating how much the designed value differs from the actual value, and $A = \frac{\omega_o}{\omega_{p,\text{DAB}}}$ denotes the ratio of the observer bandwidth to the pole frequency of the DAB, indicating how many times greater the observer's bandwidth is than the converter's pole frequency. The natural frequency of the denominator is given by

$$\omega_n = \omega_o\sqrt{K + \frac{2}{A}}, \tag{19}$$

while the quality factors are usually defined as $Q_o = 0.5$ for the numerator and (20) for the denominator.

$$Q_n = \frac{\sqrt{K + \frac{2}{A}}}{2\left(1 + \frac{1}{2A}\right)}. \tag{20}$$

In the ideal case, the nominal and actual parameters of the DAB converter are perfectly matched, resulting in $K = 1$, and the observer bandwidth becomes infinitely large, leading to $A \to \infty$. Consequently, the natural frequency of the denominator ω_n becomes equal to the natural frequency of the numerator ω_o, and the quality factor of the denominator also becomes equal to that of the numerator. As a result, the second-order terms result in cancellation, and the overall gain term $\frac{1}{\sqrt{K + \frac{2}{A}}}$ converges to 1. Therefore, (16) takes the form of a simple integrator, and with the proportional gain ω_c, it can be represented as shown in Figure 4, indicating that the larger the observer bandwidth, the better the disturbance estimation performance.
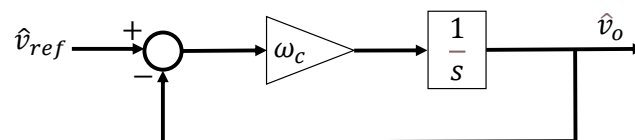

Figure 4. ADRC for DAB in the ideal case.

Conversely, when the observer bandwidth approaches zero, the quality factor associated with the denominator (20) becomes less than 0.5. Since $Q_n < 0.5$ in this case, the characteristic denominator (18) has two distinct real roots, which are given by

$$s_{1,2} = -\frac{\omega_n}{2Q_n} \pm \frac{\omega_n}{2Q_n}\sqrt{1 - 4Q_n^2}. \tag{21}$$

As A decreases, substituting (19) and (20) into (21) and simplifying shows that s_1 approaches 0 and s_2 approaches $-\omega_{p,\text{DAB}}$. Therefore, the first pole frequency ω_{p1} decreases toward zero, and the second pole ω_{p2} settles at $\omega_{p,\text{DAB}}$. This behavior can be analyzed through the Bode plot shown in Figure 5.

In Figure 5, $|N_1(j\omega)|$ represents the magnitude of the numerator term of the second-order system in (16), whereas $|1/D_1(j\omega)|$ denotes the magnitude of the second-order pole factor (i.e., the inverse of the normalized denominator). In addition, $|G_{vdo}(j\omega)|$ and $\angle G_{vdo}(j\omega)$ denote the overall magnitude and phase of (16), respectively.
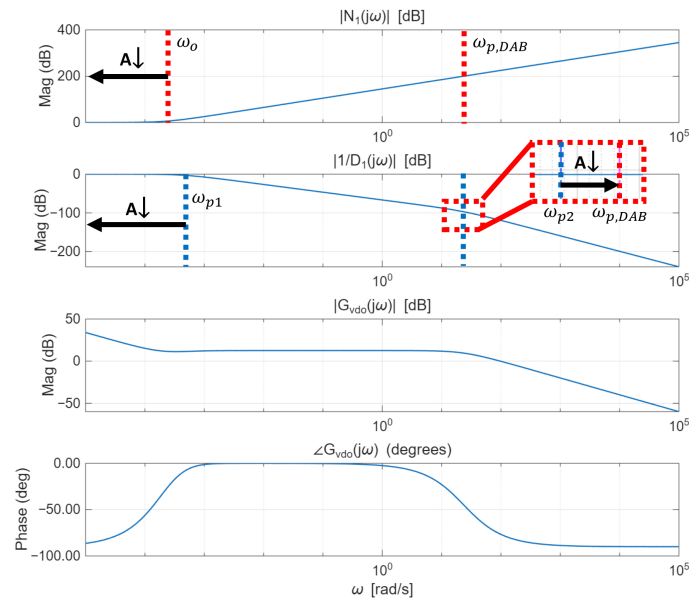

Figure 5. Bode plot of $\hat{V}_o$ with respect to $\hat{D}_o$ under a small observer bandwidth, where $A = \omega_o/\omega_{p,\text{DAB}}$ denotes the observer-bandwidth ratio. The red dotted line indicates the pole frequency of $|N_1(j\omega)|$, and the blue dotted line indicates the pole frequency of $|1/D_1(j\omega)|$.

The second-order numerator increases at a rate of 40 dB/dec around ω_o, while the first pole ω_{p1} in the denominator causes a decrease of 20 dB/dec. Subsequently, the second pole ω_{p2}, located near the DAB converter's pole frequency $\omega_{p,\text{DAB}}$, contributes an additional 40 dB/dec attenuation. When an integrator and an overall gain are added as seen in the magnitude of $G_{vdo}(j\omega)$, a flat region appears in the low-frequency range up to the second pole of the denominator. During this region, the overall gain converges to zero. Afterward, the response begins to decrease at a rate of 20 dB/dec. This indicates the formation of a mid-band gain at the crossover frequency, during which the phase margin becomes almost 180 degrees. Consequently, the low-frequency loop gain decreases, degrading disturbance rejection at low frequencies.

From Figure 3b, using Mason's rule, the relationship between the observer bandwidth and noise can be described by the output-to-disturbance transfer function (22):

$$G_{fv}(s) = \frac{\tilde{F}(s)}{\hat{V}_o(s)} = \frac{\omega_{p,\text{DAB}}}{K + \dfrac{2}{A}} \cdot \frac{N_2(s)}{D_2(s)} \tag{22}$$

where

$$N_2(s) = 1 + \frac{s}{\omega_{p,\text{DAB}}} \tag{23}$$

$$D_2(s) = 1 + \frac{1}{Q_n}\left(\frac{s}{\omega_n}\right) + \left(\frac{s}{\omega_n}\right)^2. \tag{24}$$

The output voltage $\hat{V}_o(s)$ consists of various frequency components, including ripple, load variations, and noise. The observer estimates the disturbance $\tilde{F}(s)$ based on this signal. Therefore, (22) allows the analysis of the observer's disturbance estimation characteristics in the frequency domain. Assuming the perfectly matched case ($K = 1$), the resulting Bode plot is shown in Figure 6a. The Bode plot illustrates the cases where A is 10, 100, 1000, and 10,000, and ω_{sw} denotes the switching frequency. Here, $|N_2(j\omega)|$ denotes the magnitude of the numerator term, and $|1/D_2(j\omega)|$ represents the magnitude contribution of the second-order denominator term. In addition, $|G_{fv}(j\omega)|$ indicates the overall magnitude of (22).

The magnitude of $N_2(j\omega)$ increases at 20 dB/dec for frequencies above $\omega_{p,\mathrm{DAB}}$. The contribution of the second-order denominator, $|1/D_2(j\omega)|$, corresponds to two real poles; after the first pole the slope decreases at 20 dB/dec, and after the second pole it decreases at 40 dB/dec. As A increases, the quality factor Q_n approaches 0.5, and the two real poles migrate toward $A\,\omega_{p,\mathrm{DAB}}$ according to (17) and (19), becoming nearly a repeated root. Consequently, the ESO disturbance–estimation magnitude $|G_{fv}(j\omega)|$ increases at 20 dB/dec beyond $\omega_{p,\mathrm{DAB}}$, exhibits a peak near $A\,\omega_{p,\mathrm{DAB}}$, and then decreases at 20 dB/dec. As shown in Figure 6a, when $\omega_o = 10^4\,\omega_{p,\mathrm{DAB}}$, the natural frequency ω_n lies near the switching frequency, causing the observer to treat high-frequency noise as a disturbance. As a result, the system becomes highly susceptible to noise.
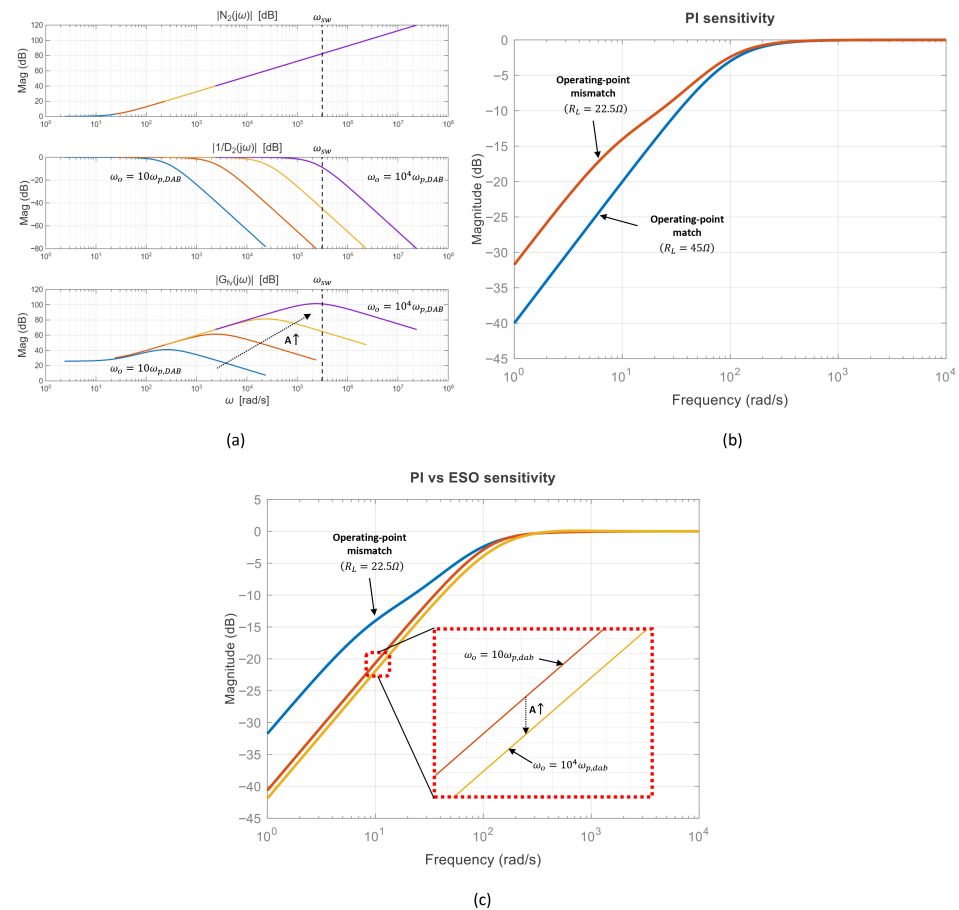

(a)

(b)

(c)

Figure 6. Unified theoretical comparison illustrating the fixed-bandwidth ESO trade-off and the expected benefit of the proposed FESO. (**a**) Bode plot of the disturbance–estimation dynamics versus $A = \omega_o/\omega_{p,\mathrm{DAB}}$ ($K = 1$). Solid curves compare $A = 10$, 100, 1000, and 10,000; the dotted arrow indicates increasing A, and the vertical dashed line denotes ω_{sw}. (**b**) Sensitivity–magnitude comparison for a PI controller under operating-point variation: matched case ($R_L = 45\ \Omega$; design point) vs. mismatched case ($R_L = 22.5\ \Omega$). (**c**) Controller comparison under the same mismatched condition ($R_L = 22.5\ \Omega$): PI vs. fixed-bandwidth ESO with different observer bandwidths ($\omega_o = 10\omega_{p,\mathrm{dab}}$, $10^4\omega_{p,\mathrm{dab}}$).

Therefore, if the bandwidth is too low, disturbances cannot be accurately estimated. On the other hand, if the bandwidth is too high, the observer becomes more vulnerable to noise. This indicates a trade-off relationship between estimation accuracy and noise robustness. Therefore, ref. [29] recommends setting the observer bandwidth ω_o to be 3 to 10 times the control bandwidth ω_c. The closed-loop transfer function in Figure 4 can be expressed as

$$\frac{1}{1 + \dfrac{s}{\omega_c}}. \tag{25}$$

Considering the 2% settling time criterion, the gain ω_c can be determined using

$$\omega_c \approx \frac{4}{T_{\text{settle}}}. \tag{26}$$

3.3. Sensitivity-Based Robustness Analysis Under Operating-Point Variations

As shown in the reduced-order model of (8), the DAB voltage plant exhibits a dominant pole at $\omega_p = 1/(R_L C_f)$, which varies significantly with the load resistance. As the load becomes lighter (R_L increases), ω_p decreases and the plant approaches an integrator. In particular, for a resistive load, the no-load operation is reported to depict a conservative (worst-case) condition for voltage-controller design [30]. Therefore, a fixed-gain controller designed at a nominal operating point may experience performance degradation when the plant deviates from the design point.

To quantify such robustness characteristics in a unified frequency-domain manner, we employ the sensitivity function

$$S(s) \triangleq \frac{1}{1 + L(s)}, \qquad L(s) = C(s)P(s) \tag{27}$$

where $P(s)$ and $C(s)$ denote the plant and controller transfer functions, respectively. Since load variations and reference changes are primarily low-frequency phenomena, the low-frequency magnitude of $|S(j\omega)|$ directly indicates disturbance-rejection capability: a smaller $|S(j\omega)|$ at low frequencies corresponds to the improved attenuation of load-induced output-voltage deviations.

Figure 6b compares the sensitivity of a fixed PI controller designed at a light-load operating point ($R_L = 45\ \Omega$) when the plant is evaluated at the design point ($R_L = 45\ \Omega$) and at a heavier-load condition ($R_L = 22.5\ \Omega$). Although the PI controller achieves the intended bandwidth at the nominal condition, the operating-point shift changes the dominant pole location ($\omega_p = 1/(R_L C_f)$) and the effective loop gain, which can increase the low-frequency sensitivity magnitude. This implies degraded rejection of load disturbances when the plant departs from the nominal design point.

Figure 6c compares the PI controller and the ESO-based controllers under the same mismatch condition (controllers designed at $R_L = 45\ \Omega$ while the plant is evaluated at $R_L = 22.5\ \Omega$). Two bandwidth settings, $\omega_o = 10\omega_{p,\text{dab}}$ and $\omega_o = 10^4\omega_{p,\text{dab}}$, are considered to illustrate the effect of ω_o on low-frequency disturbance rejection. As ω_o increases, the low-frequency sensitivity magnitude can be reduced, indicating improved attenuation of load-induced output-voltage deviations. On the other hand, the noise-related drawback of an excessively large ω_o is more directly captured by the disturbance–estimation characteristics in Figure 6a, where ω_n approaching ω_{sw} causes high-frequency ripple and noise to be treated as disturbances. These observations motivate the proposed fuzzy-bandwidth ESO, which increases ω_o only during transient load steps and decreases ω_o near steady state to avoid unnecessary noise sensitivity.

4. Proposed Fuzzy-Bandwidth ESO

As discussed in Section 3, a limitation of the conventional ESO is that its bandwidth is fixed. If the bandwidth is designed to be large in pursuit of fast response, the observer becomes more sensitive to noise. Conversely, if the bandwidth is reduced to enhance noise immunity, the disturbance estimation performance deteriorates. This reveals an inherent trade-off between the accuracy of the estimate and the robustness to noise. To overcome this limitation, this paper proposes a fuzzy logic-based ESO that adjusts the observer bandwidth in real time according to the magnitude of the estimation error.

Membership Function

The membership function in fuzzy logic is designed based on the voltage error between the actual output voltage and the voltage estimated by the ESO, and it satisfies the following rules:

- Rule 1: If e_r is VL (Very Low), then n_{fuzzy} is μ_{VL}
- Rule 2: If e_r is L (Low), then n_{fuzzy} is μ_L
- Rule 3: If e_r is M (Medium), then n_{fuzzy} is μ_M
- Rule 4: If e_r is H (High), then n_{fuzzy} is μ_H
- Rule 5: If e_r is VH (Very High), then n_{fuzzy} is μ_{VH}

Here, e_r represents the relative error between the estimated voltage $\tilde{v}_o$ from the observer and the actual output voltage $\hat{v}_o$, which is quantitatively defined as

$$e_r = \frac{|\hat{v}_o - \tilde{v}_o|}{V_{\text{ref}}} \times 100\%. \tag{28}$$

In (28), the numerator $|\hat{v}_o - \tilde{v}_o|$ represents the absolute error between the actual output voltage $\hat{v}_o$ and the estimated voltage $\tilde{v}_o$ from the observer. The denominator V_{ref} corresponds to the reference output voltage that the system aims to achieve. This allows the absolute error to be expressed as a percentage of the system reference target, allowing the design criteria to be set more intuitively and clearly.

In this paper, the error range is divided into five regions for bandwidth design, as shown in Figure 7. The error magnitude is classified into VL (Very Low), L (Low), M (Medium), H (High), and VH (Very High), depending on the output response of the system and the allowable noise range. First, when the error is within 0.1%, it is regarded as noise, where the signal mainly reflects sensor noise rather than actual disturbance, and the bandwidth is minimized to suppress noise amplification. If the error is between 0.1% and 0.5%, it is defined as the steady-state error region, representing small residual errors in which noise suppression remains a priority. An error between 0.5% and 1% is classified as the internal disturbance region, typically caused by parameter variations, and the bandwidth is moderately increased to compensate for model mismatch. An error between 1% and 2% is regarded as the external disturbance region, associated with load variations or bus impedance changes, requiring faster response through larger bandwidth. Finally, when the error exceeds 2%, it is defined as the transient region, and the bandwidth is maximized to achieve rapid disturbance rejection.
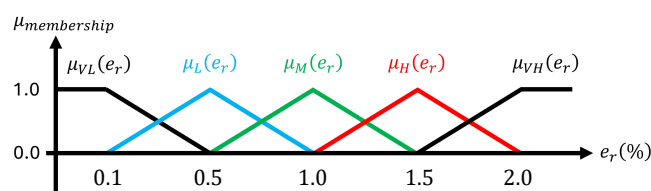

Figure 7. Membership function.

To ensure minimal computational load and latency in real-time applications, the weighted average defuzzification method is used to determine n_{fuzzy} as defined in (29):

$$n_{\text{fuzzy}} = \frac{\mu_{\text{VL}} n_{\text{VL}} + \mu_{\text{L}} n_{\text{L}} + \mu_{\text{M}} n_{\text{M}} + \mu_{\text{H}} n_{\text{H}} + \mu_{\text{VH}} n_{\text{VH}}}{\mu_{\text{VL}} + \mu_{\text{L}} + \mu_{\text{M}} + \mu_{\text{H}} + \mu_{\text{VH}}} \quad . \tag{29}$$

The value of n_{fuzzy} calculated from (29) is confined to the range $[n_{\text{VL}}, n_{\text{VH}}]$ and is employed as a gain to determine the observer bandwidth ω_o, which is defined by

$$\omega_o = n_{\text{fuzzy}} \omega_c. \tag{30}$$

The proposed FESO block diagram is illustrated in Figure 8. As shown in the figures, FESO can dynamically adjust the observer bandwidth in real time. This allows the bandwidth to increase as needed without being significantly affected by noise. Using the error between the actual output and the estimated output of the observer as input to the fuzzy logic, the observer bandwidth can be adaptively adjusted. This dynamic adjustment mechanism enables the proposed FESO to effectively overcome the limitations of conventional fixed-bandwidth ESOs.
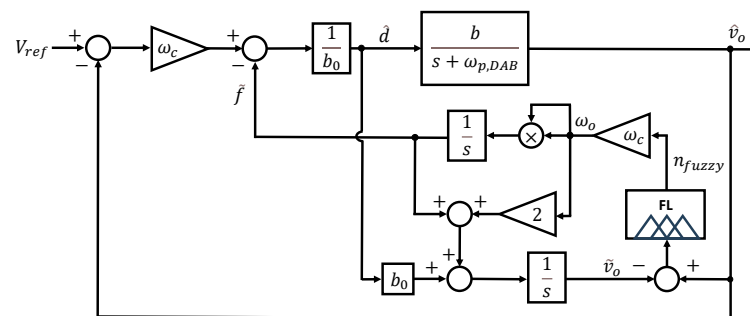

Figure 8. Block diagram of the proposed FESO.

5. Hardware Results

The hardware configuration is shown in Figure 9b. The main parameters of the DAB converter are listed in Table 1, and the control algorithm is implemented on a DSP control platform (TMS320F28379D, Texas Instruments, Dallas, TX, United States). As shown in Figure 9a, two bidirectional power supplies are used at the input and output sides: one is configured as a source, and the other as an electric load to implement the step-load condition.
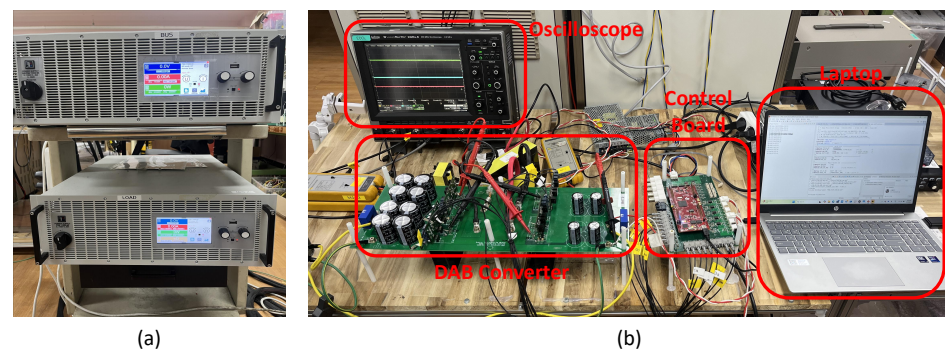

(a)   (b)

Figure 9. Hardware configuration: (**a**) bidirectional power supplies, (**b**) overall view of the DAB converter hardware setup.

Table 1. System parameters.

Parameter	Value	Parameter	Value
V_i	300 V	C_f	1880 µF
L	158 µH	N	0.5
V_{ref}	130 V	f_s	50 kHz

The hardware test was conducted under an output-voltage-controlled condition of 130 V with two step-load change scenarios. In the first scenario, the load was changed from 45 Ω to 22.5 Ω, causing the output power to increase from 375 W to 750 W. In the second scenario, the load was changed from 22.5 Ω to 45 Ω, causing the output power to decrease from 750 W to 375 W. For performance comparison with the proposed FESO, a conventional ESO and a PI controller were implemented. In the case of the conventional ESO, to achieve a settling time of 40 ms, the control bandwidth ω_c was set to 100 rad/s using (26), and the ESO bandwidth ω_o was set to 300 rad/s, three times the control bandwidth, which is typically accepted. The PI controller was designed using (8) with the pole–zero cancellation method to achieve the same settling time and a phase margin of 90°.

Figure 10 shows the waveforms of the output voltage, output current, and the primary- and secondary-side voltages of the PI controller and the conventional ESO when the load changes from 45 Ω to 22.5 Ω. Figure 10a presents the waveforms of the PI controller under a load change, showing a voltage undershoot of 4.1 V and a settling time of 45 ms. Figure 10b presents the waveforms of the conventional ESO, which exhibits a comparable voltage undershoot of 4.0 V but achieves a shorter settling time of 36 ms, approximately 9 ms faster than the PI controller. In addition, since the PI controller uses fixed gains, it cannot account for discrepancies between the parameters used in the design and the actual model, leading to degraded transient performance compared with the conventional ESO.
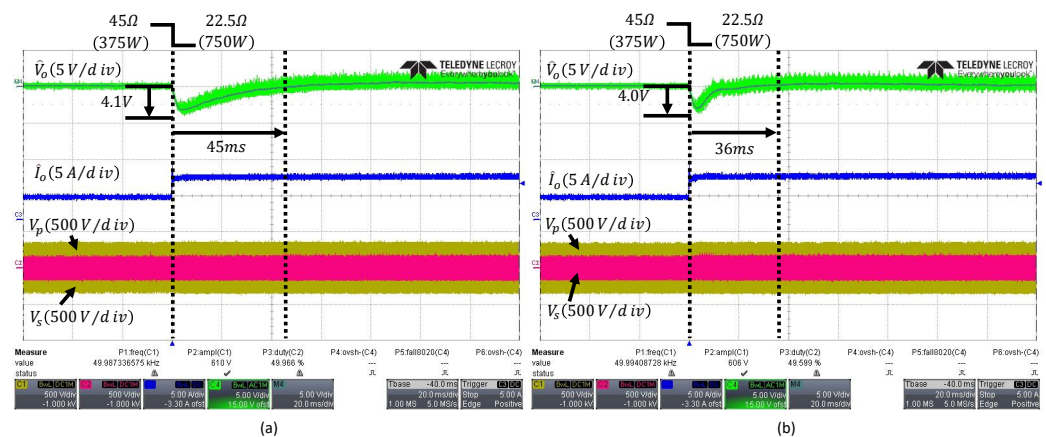

Figure 10. Transient responses to a load step from 45 Ω to 22.5 Ω: (**a**) PI controller, (**b**) conventional fixed-bandwidth ESO with $\omega_o = 300$ rad/s. The arrows indicate the peak undershoot and the settling time.

Figure 11a shows the output waveform when the observer bandwidth ω_o is set to 1500 rad/s. This corresponds to 15 times the conventional control bandwidth ω_c, which exceeds the typical range of 3 to 10 times. As the bandwidth expands, the high-frequency noise of the output voltage is amplified and reflected in the control signal, as illustrated in Figure 6a. Consequently, it can be observed that the output waveform is affected by the noise. The waveform of the proposed FESO in Figure 11b corresponds to $n_{\text{VL}} = 3$ and $n_{\text{VH}} = 15$, which define the lower and upper limits of the observer bandwidth ω_o as 300 rad/s and 1500 rad/s. The FESO operates with a low bandwidth under normal conditions to minimize noise influence and increases the bandwidth when internal or

external disturbances occur, or during transient periods, according to fuzzy logic. The FESO achieves a settling time of 23 ms and an undershoot of 3.2 V, and compared to the ESO with a fixed bandwidth of $\omega_o = 1500$ rad/s, the output waveform demonstrates that it is more robust to noise.

When the load changes from 22.5 Ω to 45 Ω, the output waveforms of the PI and ESO controller are shown in Figure 12a,b, respectively. The conventional ESO exhibits a voltage overshoot of 3.9 V and a settling time of 37 ms, whereas the PI controller shows a voltage overshoot of 4.3 V and a settling time of 55 ms, indicating that the PI controller's transient performance is inferior to that of the ESO.
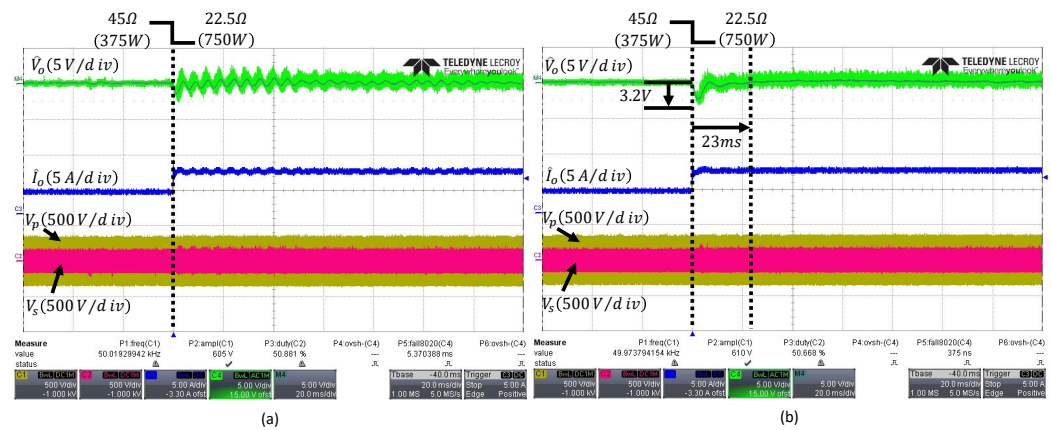
Figure 11. Transient responses under load change from 45 Ω to 22.5 Ω: (**a**) conventional fixed-bandwidth ESO with $\omega_o = 1500$ rad/s, (**b**) proposed FESO. The arrows indicate the peak undershoot and the settling time.
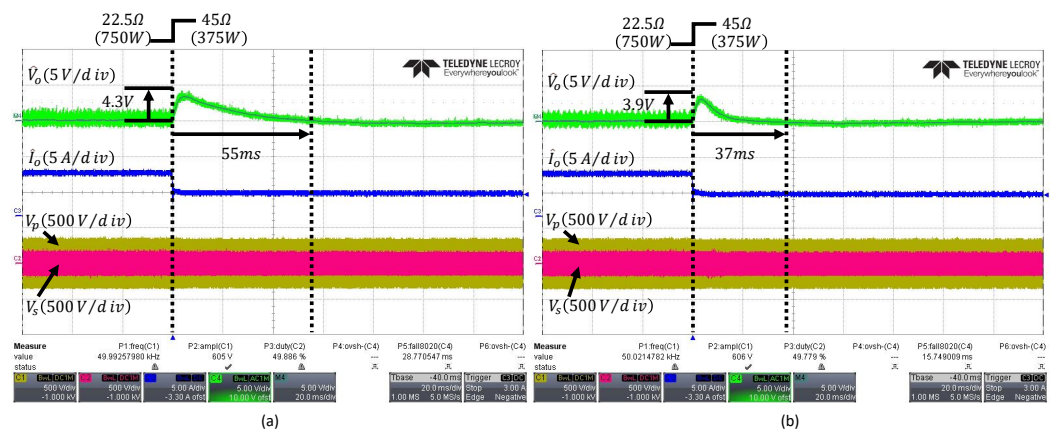

Figure 12. Transient responses under load change from 22.5 Ω to 45 Ω: (**a**) PI controller, (**b**) conventional fixed-bandwidth ESO with $\omega_o = 300$ rad/s. The arrows indicate the peak overshoot and the settling time.

Figure 13 shows the output waveform of the proposed FESO, which achieves an overshoot of 3.1 V and a settling time of 27.8 ms, demonstrating improved transient performance over the conventional controllers while minimizing the influence of noise.

Table 2 summarizes the output-voltage deviation and settling time of each controller under both load-decrease and load-increase conditions. From this table, it can be observed that the proposed FESO reduces both the voltage deviation and the settling time, thereby improving the transient performance.
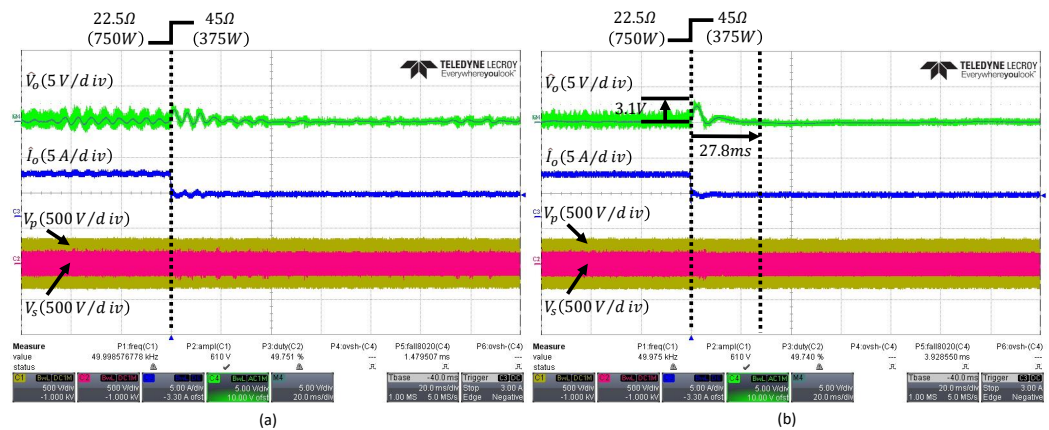
Figure 13. Transient responses under load change from 22.5 Ω to 45 Ω: (**a**) conventional fixed-bandwidth ESO with $\omega_o = 1500$ rad/s, (**b**) proposed FESO. The arrows indicate the peak overshoot and the settling time.

Table 2. Performance comparison for load-change tests.

Controller	Load Increase (375 W → 750 W)		Load Decrease (750 W → 375 W)	
	Output Voltage Undershoot	Settling Time	Output Voltage Overshoot	Settling Time
PI	4.1 V	45 ms	4.3 V	55 ms
ESO	4.0 V	36 ms	3.9 V	37 ms
FESO	3.2 V	23 ms	3.1 V	27.8 ms

6. Discussion

In this work, the proposed ESO-based disturbance compensation is implemented within the local (converter-level) digital controller of a single DAB-based ESS interface; therefore, it does not require inter-agent communication and introduces no additional communication overhead in our experimental setup. Nevertheless, if the framework is extended to networked/distributed cooperative control (e.g., higher-layer voltage restoration and power sharing), communication constraints may become an important design factor. In such cases, event-triggered strategies have been reported as an effective approach to reduce communication while maintaining closed-loop performance, e.g., the adaptive event-triggered output-feedback scheme in [31]. Exploring an event-triggered communication design for distributed extensions of the proposed local controller is an interesting direction for future work.

7. Conclusions

Based on the in-depth analysis of the trade-off associated with the bandwidth of the extended state observer (ESO), this paper proposes a Fuzzy-based ESO (FESO) with variable bandwidth to overcome the limitation of the conventional fixed-bandwidth approach. The proposed FESO adjusts the bandwidth using fuzzy logic, thereby minimizing the influence of noise while improving transient response performance. Experimental results show that, under load increase conditions, the proposed FESO reduces the output voltage undershoot by 22% and 20% compared to the conventional PI controller and ESO, respectively, and shortens the settling time by 48.9% and 36.1%. Under load decrease conditions, the output voltage overshoot is reduced by 27.9% and 20.5% compared to the PI controller and ESO, respectively, with the settling time reduced by 49.5% and 25%. These results demonstrate that the proposed FESO provides superior transient response performance compared to

conventional controllers under severe step-load conditions, thus providing ADRC for the DAB as the bidirectional power flow for the DC microgrid.

Appendix A. Derivation of the ESO Structure and Pole-Placement Gains

This appendix provides the detailed derivation of the extended state observer (ESO) used in the ADRC framework, including the error dynamics and the pole-placement gain expressions. These derivations are omitted from the main text to improve readability.

Appendix A.1. Extended-State Representation

Starting from the ADRC lumped model,

$$y^{(n)}(t) = f(t) + bu(t) \tag{A1}$$

The disturbance is augmented as an additional state to obtain the extended state representation:

$$
\begin{aligned}
\dot{x}_1(t) &= x_2(t) \\
\dot{x}_2(t) &= x_3(t) \\
&\;\;\vdots \\
\dot{x}_i(t) &= x_{i+1}(t) \\
\dot{x}_n(t) &= x_{n+1}(t) + bu(t) \\
\dot{x}_{n+1}(t) &= \dot{f}(t) \\
y(t) &= x_1(t)
\end{aligned}
\tag{A2}
$$

Appendix A.2. Luenberger-Observer Formulation

The ESO can be written in the Luenberger-observer form:

$$
\begin{aligned}
\dot{z} &= Az + Bu + L(y - Cz) \\
\tilde{y} &= Cz
\end{aligned}
\tag{A3}
$$

where the companion-form matrices are given by

$$A = \begin{bmatrix} 0 & 1 & 0 & \cdots & 0 \\ 0 & 0 & 1 & \cdots & 0 \\ \vdots & \vdots & \ddots & \ddots & \vdots \\ 0 & 0 & \cdots & 0 & 1 \\ 0 & 0 & \cdots & 0 & 0 \end{bmatrix}, \quad B = \begin{bmatrix} 0 \\ 0 \\ \vdots \\ 0 \\ b \end{bmatrix}, \quad C = \begin{bmatrix} 1 & 0 & \cdots & 0 \end{bmatrix} \tag{A4}$$

And the observer gain is

$$L = \begin{bmatrix} \beta_1 & \beta_2 & \cdots & \beta_{n+1} \end{bmatrix}^T. \tag{A5}$$

Appendix A.3. Component-Wise ESO Form

Using (A3), the ESO dynamics can be expanded as

$$\dot{z}_1(t) = z_2(t) + \beta_1\big(y(t) - z_1(t)\big)$$
$$\dot{z}_2(t) = z_3(t) + \beta_2\big(y(t) - z_1(t)\big)$$
$$\vdots$$
$$\dot{z}_i(t) = z_{i+1}(t) + \beta_i\big(y(t) - z_1(t)\big) \tag{A6}$$
$$\vdots$$
$$\dot{z}_n(t) = z_{n+1}(t) + \beta_n\big(y(t) - z_1(t)\big) + bu(t)$$
$$\dot{z}_{n+1}(t) = \beta_{n+1}\big(y(t) - z_1(t)\big).$$

Appendix A.4. Estimation Error Dynamics and Characteristic Polynomial

Define the estimation error as $e = x - z$. Neglecting $\dot{f}(t)$ for the pole-placement analysis, the error dynamics become

$$\dot{e}(t) = (A - LC)e(t). \tag{A7}$$

The characteristic equation is therefore

$$\det\big(sI - (A - LC)\big) = 0 \tag{A8}$$

which yields the polynomial form

$$s^{n+1} + \beta_1 s^n + \beta_2 s^{n-1} + \cdots + \beta_{n+1} = 0. \tag{A9}$$

Appendix A.5. Pole-Placement Gain Design

A standard ADRC/ESO pole-placement choice is to place all observer poles at $-\omega_o$, leading to

$$s^{n+1} + \beta_1 s^n + \beta_2 s^{n-1} + \cdots + \beta_{n+1} = (s + \omega_o)^{n+1}. \tag{A10}$$

Accordingly, the observer gains are obtained as

$$\beta_i = \binom{n+1}{i} \omega_o^i, \quad i = 1, 2, \ldots, n+1 \tag{A11}$$

where

$$\binom{n+1}{i} = \frac{(n+1)!}{i!(n+1-i)!}. \tag{A12}$$

As ω_o increases, the observer bandwidth increases and the estimation error converges faster; however, excessively large ω_o amplifies measurement noise and may be limited by sampling and switching-frequency constraints.

References

1. Dragičević, T.; Lu, X.; Vasquez, J.C.; Guerrero, J.M. DC Microgrids—Part II: A Review of Power Architectures, Applications, and Standardization Issues. *IEEE Trans. Power Electron.* **2016**, *31*, 3528–3549. [CrossRef]
2. Heo, K.-W.; Yun, C.-W.; Jung, G.-G.; Lee, J.-S.; Kim, H.-S.; Jung, J.-H. Enhanced Four-Port Dual-Active-Bridge Converter Employing Power Decoupling Capability for DC Microgrid Islanding Mode Operation. *J. Power Electron.* **2024**, *24*, 171–180. [CrossRef]
3. Dragičević, T.; Lu, X.; Vasquez, J.C.; Guerrero, J.M. DC Microgrids—Part I: A Review of Control Strategies and Stabilization Techniques. *IEEE Trans. Power Electron.* **2016**, *31*, 4876–4891. [CrossRef]
4. Lu, X.; Guerrero, J.M.; Sun, K.; Vasquez, J.C. An Improved Droop Control Method for DC Microgrids Based on Low Bandwidth Communication with DC Bus Voltage Restoration and Enhanced Current Sharing Accuracy. *IEEE Trans. Power Electron.* **2014**, *29*, 1800–1812. [CrossRef]
5. Hao, S.; Li, Z.; Tan, Y.; Qu, R.; Kong, W. Fast Dynamic DC-Link Voltage Control Strategy for Dual Three-Phase PM-Assisted Synchronous Reluctance Starter/Generator System. *J. Power Electron.* **2024**, *24*, 1899–1911. [CrossRef]
6. Faisal, M.; Hannan, M.A.; Ker, P.J.; Hussain, A.; Mansor, M.B.; Blaabjerg, F. Review of Energy Storage System Technologies in Microgrid Applications: Issues and Challenges. *IEEE Access* **2018**, *6*, 35143–35164. [CrossRef]
7. Jung, G.-G.; Lee, J.-S.; Kim, H.-S.; Jung, J.-H. Design Methodology of a Voltage Controller for a Dual-Active-Bridge Converter Utilizing Spread-Spectrum Modulation. *J. Power Electron.* **2025**, *25*, 393–404. [CrossRef]
8. Duong, T.-Q.; Trinh, H.-A.; Ahn, K.-K.; Choi, S.-J. Adaptive Extended State Observer for the Dual Active Bridge Converters. *Sensors* **2024**, *24*, 2397. [CrossRef]
9. Yong, S.-U.; Seo, D.; Kim, S.; Shin, J.-W.; Kim, W. Optimizing Inductance for Minimizing Reactive Power in Single-Phase-Shift Modulated Dual Active Bridge Converters under Variable Input Voltage. *J. Power Electron.* **2025**, *25*, 205–215. [CrossRef]
10. Shao, S.; Chen, L.; Shan, Z.; Gao, F.; Chen, H.; Sha, D.; Dragičević, T. Modeling and Advanced Control of Dual-Active-Bridge DC–DC Converters: A Review. *IEEE Trans. Power Electron.* **2022**, *37*, 1524–1547. [CrossRef]
11. Qin, H.; Kimball, J.W. Generalized Average Modeling of Dual Active Bridge DC–DC Converter. *IEEE Trans. Power Electron.* **2012**, *27*, 2078–2084. [CrossRef]
12. Riedel, J.; Holmes, D.G.; McGrath, B.P.; Teixeira, C. ZVS Soft Switching Boundaries for Dual Active Bridge DC–DC Converters Using Frequency Domain Analysis. *IEEE Trans. Power Electron.* **2017**, *32*, 3166–3179. [CrossRef]
13. Song, W.; Hou, N.; Wu, M. Virtual Direct Power Control Scheme of Dual Active Bridge DC–DC Converters for Fast Dynamic Response. *IEEE Trans. Power Electron.* **2018**, *33*, 1750–1759. [CrossRef]
14. Zhao, W.; Zhang, X.; Gao, S.; Ma, M. Improved Model-Based Phase-Shift Control for Fast Dynamic Response of Dual Active Bridge DC/DC Converters. *IEEE J. Emerg. Sel. Top. Power Electron.* **2020**, *9*, 223–231. [CrossRef]
15. Hassan, M.A.; Su, C.-L.; Pou, J.; Sulligoi, G.; Almakhles, D.; Bosich, D.; Guerrero, J.M. DC Shipboard Microgrids with Constant Power Loads: A Review of Advanced Nonlinear Control Strategies and Stabilization Techniques. *IEEE Trans. Smart Grid* **2022**, *13*, 3422–3438. [CrossRef]
16. Tarisciotti, L.; Chen, L.; Shao, S.; Dragičević, T.; Wheeler, P.; Zanchetta, P. Finite Control Set Model Predictive Control for Dual Active Bridge Converter. *IEEE Trans. Ind. Appl.* **2022**, *58*, 2155–2165. [CrossRef]
17. Chen, L.; Shao, S.; Xiao, Q.; Tarisciotti, L.; Wheeler, P.W.; Dragičević, T. Model Predictive Control for Dual-Active-Bridge Converters Supplying Pulsed Power Loads in Naval DC Micro-Grids. *IEEE Trans. Power Electron.* **2020**, *35*, 1957–1966. [CrossRef]
18. Chen, L.; Gao, F.; Shen, K.; Wang, Z.; Tarisciotti, L.; Wheeler, P.; Dragičević, T. Predictive Control Based DC Microgrid Stabilization with the Dual Active Bridge Converter. *IEEE Trans. Ind. Electron.* **2020**, *67*, 8944–8956. [CrossRef]
19. Yin, Z.; Deng, F.; Kaddah, S.S.; Ghanem, A.; Abulanwar, S.; Zhang, Y. Finite-Control-Set Model-Free Predictive Control Based on Voltage Noise Suppression for Dual Active Bridge Converters. *J. Power Electron.* **2025**, *25*, 1309–1319. [CrossRef]
20. Kang, Z.; Li, Y. Active Disturbance Rejection Control of Full-Bridge DC–DC Converter for a Pulse Power Supply with Controllable Charging Time. *Electronics* **2023**, *12*, 5018. [CrossRef]
21. Mosayebi, M.; Sadeghzadeh, S.M.; Gheisarnejad, M.; Khooban, M.H. Intelligent and Fast Model-Free Sliding Mode Control for Shipboard DC Microgrids. *IEEE Trans. Transp. Electr.* **2021**, *7*, 1662–1671. [CrossRef]
22. Sami, I.; Alhosaini, W.; Khan, D.; Ahmed, E.M. Advancing Dual-Active-Bridge DC–DC Converters with a New Control Strategy Based on a Double Integral Super Twisting Sliding Mode Control. *World Electr. Veh. J.* **2024**, *15*, 348. [CrossRef]
23. Guo, H.; Xiang, T.; Liu, Y.; Zhang, Q.; Liu, S.; Guan, B. Active Disturbance Rejection Control Method for Marine Permanent-Magnet Propulsion Motor Based on Improved ESO and Nonlinear Switching Function. *J. Mar. Sci. Eng.* **2023**, *11*, 1751. [CrossRef]

24. Gao, Z. Active Disturbance Rejection Control: A Paradigm Shift in Feedback Control System Design. In Proceedings of the 2006 American Control Conference, Minneapolis, MN, USA, 14–16 June 2006. . [CrossRef]

25. Chen, W.; Yang, J.; Guo, L.; Li, S. Disturbance-Observer-Based Control and Related Methods—An Overview. *IEEE Trans. Ind. Electron.* **2016**, *63*, 1083–1095. [CrossRef]

26. Łakomy, K.; Madonski, R.; Dai, B.; Yang, J.; Kicki, P.; Li, S. Active Disturbance Rejection Control Design with Suppression of Sensor Noise Effects in Application to DC–DC Buck Power Converter. *IEEE Trans. Ind. Electron.* **2021**, *69*, 816–824. [CrossRef]

27. Guo, B.; Bacha, S.; Alamir, M.; Hably, A.; Boudinet, C. Generalized Integrator–Extended State Observer with Applications to Grid-Connected Converters in the Presence of Disturbances. *IEEE Trans. Control Syst. Technol.* **2021**, *29*, 744–755. [CrossRef]

28. Wang, S.; Gan, H.; Luo, Y.; Luo, X.; Chen, Y. A Fractional-Order ADRC Architecture for a PMSM Position Servo System with Improved Disturbance Rejection. *Fractal Fract.* **2024**, *8*, 54. [CrossRef]

29. Benrabah, A.; Xu, D.; Gao, Z. Active Disturbance Rejection Control of LCL-Filtered Grid-Connected Inverter Using Padé Approximation. *IEEE Trans. Ind. Appl.* **2018**, *54*, 6179–6189. [CrossRef]

30. Krismer, F.; Kolar, J.W. Accurate Small-Signal Model for the Digital Control of an Automotive Bidirectional Dual Active Bridge. *IEEE Trans. Power Electron.* **2009**, *24*, 2756–2768. [CrossRef]

31. Liu, G.; Liang, H.; Wang, R.; Sui, Z.; Sun, Q. Adaptive Event-Triggered Output Feedback Control for Nonlinear Multiagent Systems Using Output Information Only. *IEEE Trans. Syst. Man Cybern. Syst.* **2025**, *55*, 7639–7650. [CrossRef]